

MULTI-FIDELITY BAYESIAN NEURAL NETWORKS FOR STEALTH/AERODYNAMIC DATA FUSION METHOD

Jiayi He[1], Huan Zhao[2]

[1-2] School of Aeronautics, Northwestern Polytechnical University, Xi'an Shaanxi, 710072, China

Abstract

To address the trade-off between accuracy and efficiency in numerical methods for stealth characteristic evaluation, as well as the overfitting tendency of traditional neural networks under small-sample conditions, a multi-source stealth data fusion method based on a multi-fidelity Bayesian neural network is proposed. The method employs a hierarchical architecture: a deep neural network is used to fit low-fidelity Physical Optics data, while a Bayesian neural network combined with an improved variational inference learns the nonlinear mapping between high- and low-fidelity data and quantifies predictive uncertainty. The proposed method is validated using multiple standard test functions, three-dimensional electromagnetic stealth data of the flying-wing X47B configuration, and unsteady aerodynamic data of the NACA0012 airfoil. The results demonstrate that, under the same numbers of high- and low-fidelity samples, the proposed method achieves significantly lower mean square error and higher coefficient of determination compared to the traditional Co-Kriging method. Its uncertainty distribution avoids redundant coverage and reasonably widens in extrapolation regions without data, and its predicted aerodynamic mean values align more closely with wind tunnel test data. The proposed method provides an efficient, high-fidelity, and uncertainty-aware modeling tool for multidisciplinary analysis and optimization design of aircraft.

Keywords: Electromagnetic Stealth Characteristics; Data Fusion; Multi-fidelity Surrogate Model; Bayesian Neural Network; Aerodynamic Characteristics

1. General Introduction

In the aircraft design phase, obtaining stealth characteristic parameters such as Radar Cross Section (RCS) primarily relies on theoretical simulation. However, existing electromagnetic numerical computation methods still face an inherent trade-off between rapidity and accuracy: numerical methods represented by the Method of Moments (MoM) offer high computational accuracy, but their computational complexity increases dramatically with the number of discretized elements; high-frequency methods represented by Physical Optics (PO) are computationally fast and suitable for engineering estimation, yet they suffer from insufficient accuracy when dealing with scattering problems involving complex targets.

To address these limitations, data fusion combined with surrogate modeling techniques has garnered widespread attention. Currently, the most commonly studied methods for constructing surrogate models include Polynomial Response Surface Method (PRSM)[1], Support Vector Machine (SVM)[2], Radial Basis Function, Gaussian Random Process, Kriging method[3], and Artificial Neural Network (ANN), among others. Building Multi-fidelity Surrogate Models (MFSM) based on data fusion can significantly reduce modeling time and computational cost, and has important applications in engineering optimization, computational fluid dynamics, materials science, multi-objective optimization,

and uncertainty quantification. For example, Espoeys et al.[4] proposed a multi-fidelity Bayesian optimization method for reliability assessment of complex systems. By constructing a multi-fidelity surrogate model combined with constraint function optimization, this method improves the efficiency of reliability assessment. Zhang et al.[5] employed a self-supervised learning method to train a physics-driven deep multi-fidelity model (PD-DMFM), which fully leverages the physical characteristics of engineering systems and reduces the reliance on large amounts of low-fidelity data during training. Jofre et al.[6] evaluated the performance of a range of different multi-fidelity strategies and modeling methods to propagate uncertainties encountered in irradiated particle-laden turbulence associated with volumetric solar receivers.

In the field of aircraft design, multi-fidelity surrogate models are predominantly applied to aerodynamic optimization. Wang et al.[7] constructed a data fusion framework for flight tests based on the random forest method. Zhao et al.[8] made full use of pressure distribution information generated during sampling to improve modeling accuracy and generalization, thereby reducing the cost of sample acquisition. Peng et al.[9] improved a modeling framework based on hierarchical Kriging for nonlinear aerodynamic reduced-order modeling, providing reliable uncertainty estimates for predicted unsteady aerodynamic characteristics. Li et al.[10] established a multi-fidelity aerodynamic model based on Deep Neural Networks (DNN) for aerodynamic pressure distribution on wing surfaces, incorporating both numerical and experimental data into the loss function with appropriate weighting factors to balance overall accuracy.

The modeling methods for multi-fidelity surrogate models have consistently been a research hotspot. Park et al.[11] compared the characteristics of different MFSM frameworks and evaluated their performance. Existing modeling methods primarily include additive correction[12, 13], multiplicative correction[14, 15], comprehensive correction[16], and space mapping[17]. Among these, the most widely used is the Co-Kriging method proposed by Kennedy and O'Hagan[18], which is regarded as a technique for constructing high-fidelity approximations enhanced by low-fidelity data. It assumes zero covariance between high- and low-fidelity data and employs an autoregressive model to model their discrepancy. By maximizing the log marginal likelihood, this method simultaneously identifies parameters and hyperparameters, thereby improving prediction accuracy and efficiency. Chung et al.[19] explored the application of the Co-Kriging method in supersonic business jet design. Zhang et al.[20] applied the Co-Kriging method to construct a surrogate model for the aerodynamic performance of high-altitude propellers. Huang et al.[21] compared the characteristics of the Co-Kriging multi-fidelity model with those of traditional Kriging-based multi-fidelity models using a wing-body integration aircraft as an example. However, conventional data fusion methods struggle with high-dimensional and highly nonlinear problems. Consequently, artificial intelligence methods, particularly neural networks, have begun to be applied to data fusion. Research has shown that neural networks, through their autonomous feature learning mechanism, can effectively capture complex correlations between data of different fidelities, avoiding the error accumulation of traditional weighted fusion methods under specific operating conditions. For example, Meng et al.[22] proposed a multi-fidelity composite neural network that combines DNN and Physics-informed Neural Network (PINN), capable of adaptively learning both linear and complex nonlinear correlations between low- and high-fidelity data. Li et al.[23] proposed a DNN-based multi-fidelity Bayesian optimization method that captures complex relationships between different fidelities through a flexible neural network architecture, thereby improving surrogate model accuracy. Lee et al.[24] introduced a novel framework using graph neural networks to solve multi-agent perimeter defense problems, where the deep neural network is trained in a supervised manner using an expert strategy based on a maximum matching algorithm.

The aforementioned multi-fidelity deep neural network models often lack interpretability, and their generalization ability is insufficient, leading to unpredictable and overconfident behavior on data points outside the training distribution. To address this, Bayesian Neural Networks (BNNs) have attracted considerable attention. By introducing Bayesian inference into neural networks, BNNs enable uncertainty quantification, thereby providing greater robustness and interpretability when dealing with complex problems. Xie et al.[25] applied BNNs to multi-source aerodynamic data fusion with heterogeneous uncertainties, significantly improving fusion accuracy and outperforming multi-fidelity Gaussian process regression models. Vaiuso et al.[26] combined BNNs with a transfer learning framework to provide both predictions and confidence estimates. Yang et al.[27] proposed Bayesian

physics-informed neural networks to solve forward and inverse nonlinear problems described by partial differential equations with noisy data, leveraging physical laws and scattered noise measurements to predict and quantify aleatoric uncertainty arising from noisy data within a Bayesian framework. Compared with PINNs, Bayesian physics-informed neural networks achieve not only uncertainty quantification but also more accurate predictions in high-noise scenarios. However, posterior inference in BNNs remains challenging. For complex models, directly sampling from the posterior distribution is extremely difficult due to the high dimensionality of the sampling space. The most popular algorithm, Markov Chain Monte Carlo (MCMC), can sample the posterior exactly but lacks scalability due to the need to store a large number of samples.

In summary, to address the limitations of existing multi-fidelity surrogate models under high-dimensional and highly nonlinear conditions, the lack of reasonable uncertainty characterization in traditional neural networks, and the difficulty of high-dimensional posterior sampling in Bayesian neural networks, this paper establishes a Multi-fidelity Bayesian Neural Network (MFBNN) model. This model combines the nonlinear fitting capability of deep neural networks with the fusion characteristics of multi-source, multi-fidelity electromagnetic data, overcoming the issues of data scarcity and over-reliance on high-fidelity models in electromagnetic problems. Furthermore, it employs Variational Inference (VI) to approximate the true posterior distribution, thereby avoiding the complexity of high-dimensional posterior sampling and significantly reducing computational cost. In addition to its successful application to electromagnetic characteristic data fusion, the proposed model is further extended to the field of aerodynamic characteristics, providing a unified modeling framework for multi-fidelity data fusion across two different physical scenarios. Validation using multiple standard test functions, three-dimensional electromagnetic stealth data of the X47B flying-wing configuration, and unsteady aerodynamic data of the NACA0012 airfoil, followed by comparative analysis with the traditional Co-Kriging method, demonstrates that the proposed model not only effectively reduces reliance on high-fidelity samples and significantly improves modeling efficiency, but also achieves a breakthrough in prediction accuracy. It outperforms Co-Kriging in capturing local features of complex configurations and provides more reasonable uncertainty intervals.

2. Model Framework

2.1 Bayesian Neural Network

BNN is an artificial neural network trained using Bayesian inference. Compared to traditional point-estimate networks, a BNN, whose weights follow probability distributions, estimates uncertainty over the relevant probability distribution by comparing the predictions of multiple sampled models, and can ultimately address the overfitting problem under small-sample conditions. If the predictions from different models are consistent, the uncertainty is low; if the predictions are inconsistent, the uncertainty is high. This process can be summarized as:

$$\begin{aligned} \theta &\sim P(\theta) \\ y &= \Phi(\theta) + \varepsilon \end{aligned} \tag{1}$$

where θ represents the network weights w and biases b, denoted as $\theta = (w, b)$, ε is random noise, indicating that Φ is only an approximation.

The first step in designing a BNN is to select a functional model that maps the relationship between inputs and outputs. Then, a stochastic model needs to be chosen, namely the prior distribution of possible model parameters $P(\theta)$ and the prior confidence in the model's predictive capability $P(y \mid x, \theta)$. Let D represent the training set, with D_x and D_y denoting the training inputs and outputs, respectively. Applying Bayes' theorem and assuming that the model parameters and inputs are independent, the Bayesian posterior probability can be written as:

$$P(\theta \mid D) = \frac{P(D_y \mid D_x, \theta) P(\theta)}{\int_{\theta'} P(D_y \mid D_x, \theta') P(\theta') d\theta'} \simeq P(D_y \mid D_x, \theta) P(\theta) \tag{2}$$

Since the posterior probability is a high-dimensional and highly non-convex probability distribution, and the evidence is extremely difficult to compute, two mainstream posterior inference methods are introduced to estimate the true posterior: MCMC methods and VI methods.

The fundamental idea of the MCMC algorithm is to construct a Markov chain of samples S_i, where the

probability of the next sample S_{i+1} depends only on the current sample S_i. By constructing a Markov chain with a specific transition kernel, its stationary distribution is made to exactly equal the desired target posterior distribution, i.e., $P(\theta \mid D)$. In the actual sampling process, the MCMC method exhibits two key dynamic characteristics. Samples from the initial phase (called the "burn-in" period) are typically discarded because the Markov chain has not yet reached a stationary distribution. Moreover, due to the complex correlation structures that usually exist among neural network parameters, the speed at which MCMC explores the entire posterior distribution in the ultra-high-dimensional parameter space of BNNs is often slow. Nevertheless, because of its high accuracy, this method remains widely used. Another important phenomenon during sampling is the autocorrelation of samples. Since the current state of the Markov chain depends on the previous state, adjacent samples are often highly correlated, resulting in an effective sample size that is usually much smaller than the actual number of samples. Therefore, in BNN applications, a sparse sampling strategy is often adopted, i.e., retaining only one sample for every *k* samples, to reduce storage burden and improve computational efficiency.

The MCMC algorithm is the best tool for sampling from exact posterior distributions, but it lacks scalability when the model size becomes large. VI is more widely used than the MCMC algorithm. Its core idea is to introduce a distribution $q_\phi(\theta)$ controlled by parameters ϕ, called the variational distribution, and to make the variational distribution $q_\phi(\theta)$ as close as possible to the exact posterior by learning the values of the parameters ϕ. The Kullback-Leibler (KL) divergence is a measure of the closeness between the two distributions. For Bayesian inference, its calculation formula is:

$$D_{KL}(q_\phi(\theta) \| P) = \int_\theta q_\phi(\theta) \log\left(\frac{q_\phi(\theta)}{P(\theta \mid D)}\right) d\theta \tag{3}$$

To avoid directly computing $P(\theta \mid D)$, the Evidence Lower Bound (ELBO) is introduced as the loss function. First, substituting the posterior expression (2) into equation (3) yields:

$$\begin{aligned} D_{\mathrm{KL}}(q_\phi \| P) &= \mathbb{E}_{q_\phi}\left[\log q_\phi(\theta)\right] - \mathbb{E}_{q_\phi}\left[\log P(\theta \mid D)\right] \\ &= \mathbb{E}_{q_\phi}\left[\log q_\phi(\theta)\right] - \mathbb{E}_{q_\phi}\left[\log P(D \mid \theta)\right] \\ &\quad - \mathbb{E}_{q_\phi}\left[\log P(\theta)\right] + \log P(D) \end{aligned} \tag{4}$$

Note that $\log P(Y \mid X)$ does not depend on ϕ. Rearranging the terms gives:

$$\log P(D) = \mathbb{E}_{q_\phi}\left[\log P(D \mid \theta)\right] - D_{\mathrm{KL}}(q_\phi \| P(\theta)) + D_{\mathrm{KL}}(q_\phi \| P(\theta \mid D)) \tag{5}$$

where ELBO is defined as:

$$\mathrm{ELBO}(\phi) = \mathbb{E}_{q_\phi}\left[\log P(D \mid \theta)\right] - D_{\mathrm{KL}}(q_\phi \| P(\theta)) \tag{6}$$

Thus, equation (5) can be written as:

$$\mathrm{ELBO}(\phi) = \log P(D) - D_{\mathrm{KL}}(q_\phi \| P(\theta \mid D)) \tag{7}$$

Since $\log P(Y \mid X)$ depends only on the prior conditions, minimizing the KL divergence is equivalent to maximizing the ELBO.

2.2 MFBNN Model Architecture

Based on the above theoretical foundation, the proposed MFBNN model is constructed in Figure 1. The first is a traditional DNN used to approximate low-fidelity data. Since low-fidelity data typically have a sufficient number of samples, using a BNN on top of them would incur extremely high computational costs. Therefore, to achieve high computational efficiency, this paper employs Maximum A Posteriori (MAP) estimation to train the first neural network, without the need to quantify its uncertainty. Consequently, every hyperparameter in this neural network is a point estimate rather than a distribution. The loss function of MAP is expressed as:

$$\mathcal{L}_L = \frac{1}{N_L} \mid y_L - \tilde{y}_L \mid^2 + \alpha \mid w_L \mid^2 \tag{8}$$

Where N_L is the number of low-fidelity training data points, $y_L^{(i)}$ and $\tilde{y}_L^{(i)}$ are the low-fidelity training data and predicted values, respectively. The second term is the L_2 regularization term, where w_L represents the weights in the first DNN, and α is the regularization weight. L_2 regularization can reduce

overfitting caused by measurement noise as well as by the deep neural network itself.

The second model is a Bayesian neural network, which is used to learn the correlation between low-fidelity and high-fidelity data and to quantify the uncertainty of the neural network model. Taking $\tilde{y}_L$ as input, and given the prior distribution, equation (2) can be written as:

$$P(\theta \mid D_H) = \frac{P(u_H \mid \{\tilde{u}_L, x_H\}, \theta)P(\theta)}{\int_\theta P(u_H \mid \{\tilde{u}_L, x_H\}, \theta')P(\theta')d\theta'} \simeq P(u_H \mid \{\tilde{u}_L, x_H\}, \theta)P(\theta) \tag{9}$$

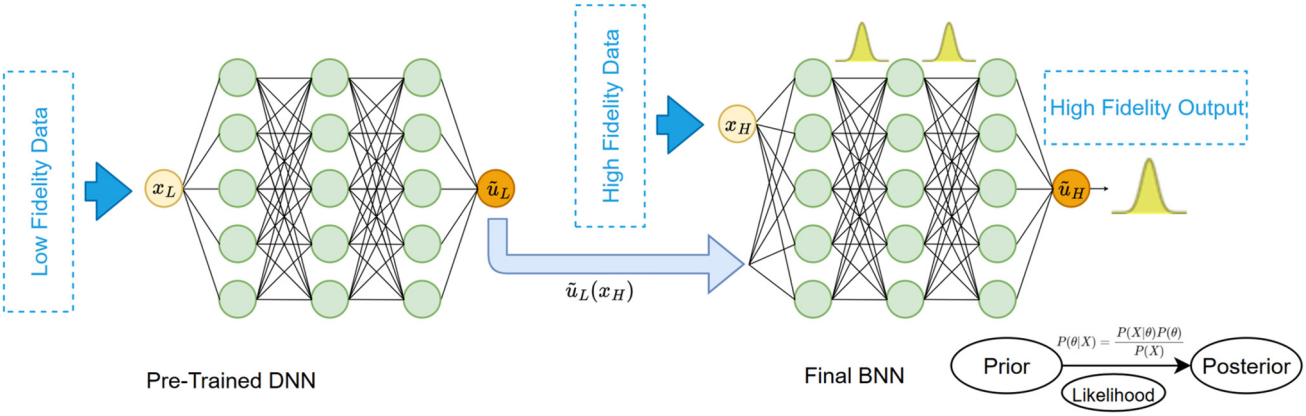


Figure 1 – Multi-fidelity Bayesian neural network model architecture.

2.3 VI Optimization

In the model proposed in this paper, VI is chosen as the posterior estimation method. The goal of VI is to maximize the ELBO, so the loss function is designed as the negative of the ELBO, i.e.:

$$\mathcal{L}(\theta) = \mathbb{E}_{q_\phi}[-\log P(D \mid \theta)] + D_{KL}(q_\phi \mid\mid P(\theta)) \tag{10}$$

The optimization problem is:

$$\theta^* = \arg\max_\theta \ \mathrm{ELBO}(\theta) = \arg\min_\theta \mathcal{L}(\theta) \tag{11}$$

The first term in equation (10) is the likelihood term. From equation (1), assuming that the error between the model output $\hat{y}$ and the true value y follows a Gaussian distribution:

$$u_H = \tilde{u}_H + \epsilon, \quad \epsilon \sim \mathcal{N}(0, \sigma^2) \tag{12}$$

Where ϵ is the noise term with mean 0 and variance σ^2. At this point, the data likelihood $P(Y \mid X, \theta)$ is expressed as:

$$P(u_H \mid \{\tilde{u}_L, x_H\}, \theta) = \frac{1}{\sqrt{2\pi\sigma^2}} \exp\left(-\frac{(u_H - \tilde{u}_H)^2}{2\sigma^2}\right) \tag{13}$$

The final objective is simplified to:

$$\mathbb{E}_{q_\phi}[-\log P(D \mid \theta)] \propto \frac{1}{2\sigma^2} \sum_{i=1}^{N} \left(u_{Hi} - \tilde{u}_{Hi}\right)^2 \tag{14}$$

where the scaling factor $\frac{1}{2\sigma^2}$ can be regarded as a weight, so the likelihood term can be written in the form of Mean Square Error (MSE):

$$\mathrm{MSE} = \frac{1}{N} \sum_{i=1}^{N} \left(u_{Hi} - \tilde{u}_{Hi}\right)^2 \tag{15}$$

This term is often used as an evaluation metric for model fitting ability. Similar metrics include Root Mean Square Error (RMSE):

$$\mathrm{RMSE} = \sqrt{\mathrm{MSE}} = \sqrt{\frac{1}{N} \sum_{i=1}^{N} \left(u_{Hi} - \tilde{u}_{Hi}\right)^2} \tag{16}$$

and the coefficient of determination R^2:

$$R^2 = 1 - \frac{\sum_{i=1}^{N} \left(u_{Hi} - \tilde{u}_{Hi}\right)^2}{\sum_{i=1}^{N} \left(u_{Hi} - \bar{u}\right)^2} \tag{17}$$

Where $\bar{u}$ is the mean of the true values.

The second term in equation (8) can be viewed as a regularization term, which describes the difference between the variational distribution and the prior distribution. The standard practice is to use a normal prior with mean 0.

VI provides an excellent mathematical tool for Bayesian inference, but it needs to be adapted to deep learning. The main issue is that stochasticity prevents backpropagation from functioning properly at the internal nodes of the neural network. This paper focuses on the Bayesian backpropagation method, which combines stochastic VI with the reparameterization trick to ensure that backpropagation can work properly. The idea is to represent the random variable θ as a deterministic function:

$$\theta = \mu + \sigma \odot \epsilon, \quad \epsilon \sim \mathcal{N}(0,1) \tag{18}$$

Thus, the gradient can be propagated to μ and σ:

$$\nabla_\theta \mathbb{E}_{q_\phi(\theta)}[\tilde{u}_H(\theta)] = \mathbb{E}_{\epsilon \sim \mathcal{N}(0,1)}[\nabla_\theta \tilde{u}(\mu + \sigma \odot \epsilon)] \tag{19}$$

During optimization, Stochastic Gradient Descent (SGD) is used. The gradient of the likelihood term is estimated using mini-batch data, and the KL term can be estimated through sampling. Therefore, we have:

$$\nabla_\theta \mathrm{ELBO} \approx \frac{N}{M} \sum_{i \in batch} \left\{ \nabla_\theta \log P(D \mid \theta) - \nabla_\theta D_{KL}\left(q_\phi \,\|\, P(\theta)\right) \right\} \tag{20}$$

Where N is the total amount of data, and M is the batch size. For the KL term, Monte Carlo sampling is used:

$$D_{KL}\left(q_\phi \,\|\, P(\theta)\right) = \frac{1}{K} \sum_{k=1}^{K} \log q(\theta_k) - \log P(\theta_k) \qquad \theta_k \sim q_\phi(\theta) \tag{21}$$

The optimization process of VI is essentially searching for the optimal approximation in the probability distribution space, efficiently implemented through reparameterization and SGD, which can significantly improve scalability and computational efficiency.

3. Multi-fidelity Function Tests

Bayesian neural networks are capable of estimating uncertainty, which is divided into aleatoric uncertainty and epistemic uncertainty. Aleatoric uncertainty arises from the inherent noise or randomness in the data itself and cannot be eliminated even by collecting more data or improving the model; it is typically encoded as part of the likelihood term. Epistemic uncertainty stems from the model's own lack of knowledge, such as insufficient training data or inadequate model complexity. This type of uncertainty decreases as the amount of data increases or the model is improved. In BNNs, it is encoded in the posterior probability, representing the uncertainty due to lack of data and reflecting the model's confidence in its predictions. Therefore, this uncertainty can also be viewed as model variance, which can be captured through the range of possible functions and the probability assigned to each function. Combining these two types of uncertainty yields the total uncertainty. Bayesian neural networks model epistemic uncertainty and aleatoric uncertainty separately, where epistemic uncertainty is modeled as $P(\theta|D_H)$ and aleatoric uncertainty is modeled as $P(u_H|\{\tilde{u}_L, x_H\}, \theta)$.

3.1 Typical 1D Test Function

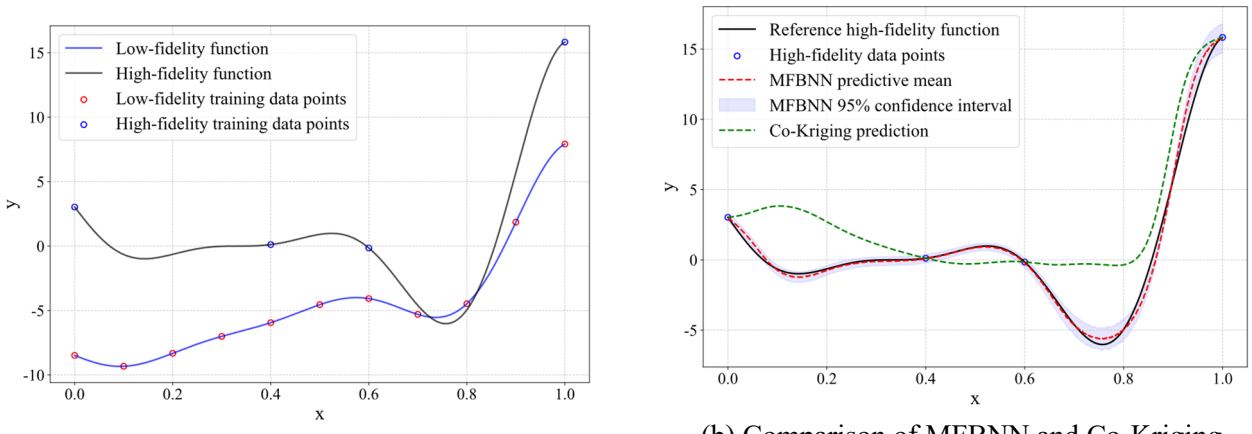
Consider an example of data approximation for a continuous one-dimensional function based on two fidelity levels, where the low-fidelity and high-fidelity data are generated from the following functions:

$$\begin{cases} y_H(x) = (6x-2)^2 \sin(12x-4) \\ y_L(x) = A y_H(x) + B(x-0.5) + C \end{cases} \quad x \in [0,1] \tag{22}$$

In the equations, y_H has a linear relationship with y_L, and $\mathrm{A} = 0.5, \mathrm{B} = 10, \mathrm{C} = -5$. As shown in Figure

2(a), there are 11 low-fidelity training data points distributed as $x_L = \{0,0.1,0.2,0.3,0.4,0.5,0.6,0.7,0.8,0.9,1.0\}$ and 4 high-fidelity training data points distributed as $x_H = \{0,0.4,0.6,1.0\}$.

First, only low-fidelity data are used to predict the low-fidelity function. Here, the DNN uses 6 hidden layers with 64 neurons per layer and no regularization. Second, for the BNN high-fidelity model, only one hidden layer with 100 neurons is used, and the KL weight, i.e., the regularization rate, is set to 1e-6. The final predicted mean and 95% confidence interval are shown in Figure 2(b). It can be observed that the BNN predicted mean agrees well with the actual high-fidelity function. Furthermore, the figure also plots the predicted posterior mean of the Co-Kriging method, which intuitively shows that MFBNN outperforms the traditional Co-Kriging model in prediction accuracy. Unlike Co-Kriging, the MFBNN does not require prior knowledge about the correlation between low-fidelity and high-fidelity data, indicating that the proposed model can dynamically learn the correlation from the given data.



(a) Distribution of high and low-fidelity data

(b) Comparison of MFBNN and Co-Kriging predictions

Figure 2 – Regression with typical 1D test functions

3.2 Highly nonlinear 1D test function

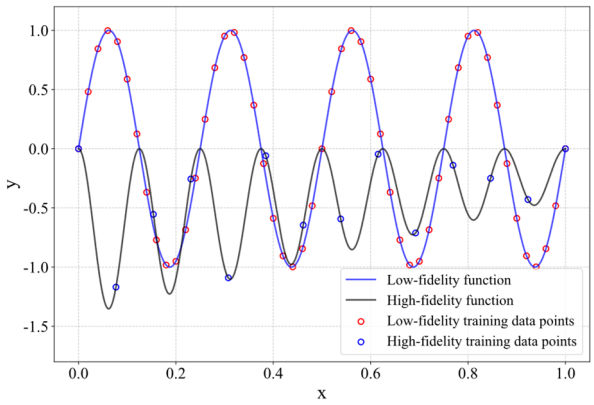
To further investigate the complex relationship between data of different fidelity levels, the following nonlinearly correlated function is considered:

$$\begin{cases} y_L(x) = \sin(8\pi x) \\ y_H(x) = (x-\sqrt{2})y_L^2(x) \end{cases} \quad x \in [0,1] \tag{23}$$

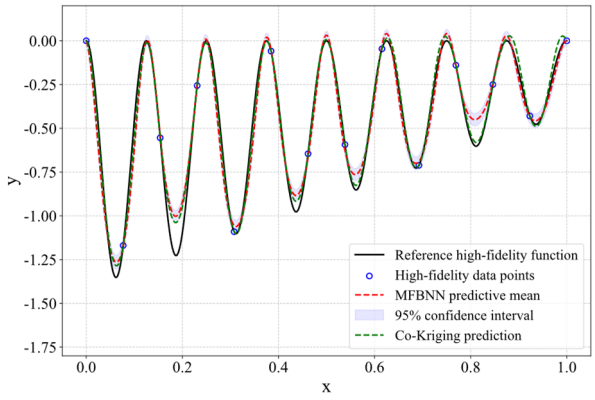
Fifty uniformly distributed data points and fourteen uniformly distributed data points in the interval [0, 1] are used as low-fidelity and high-fidelity training data, respectively (as shown in Figure 3(a)). The low-fidelity DNN model uses 4 hidden layers with 20 neurons per layer. For the BNN, a single hidden layer with 50 neurons is used, and the regularization rate is also set to 1e-6.

The results of multi-fidelity modeling are shown in Figure 3(b). A comparison of relevant metrics between MFBNN and Co-Kriging is presented in Table 1. The mean square error of MFBNN is significantly smaller than that of Co-Kriging, indicating better prediction accuracy.

Although the trend of low-fidelity data is opposite to that of high-fidelity data in some regions (e.g., when $0 < x < 0.2$, the low- and high-fidelity levels exhibit opposing patterns), MFBNN can still provide accurate predictions for the high-fidelity configuration. Moreover, the error between the predicted mean and the exact solution is largely bounded by two standard deviations across the entire region.



(a) Distribution of high and low-fidelity data



(b) Comparison of MFBNN and Co-Kriging predictions

Figure 3 – Regression with nonlinear 1D test functions

Table 1 – Comparison of evaluation metrics for regression with highly nonlinear 1D test function

Model	MSE	RMSE	R^2
MFBNN	0.001515	0.038924	0.988812
Co-Kriging	0.003476	0.058960	0.974330

3.3 4D Test Function

This section considers a four-dimensional function regression problem. The multi-fidelity training data are generated by the following functions:

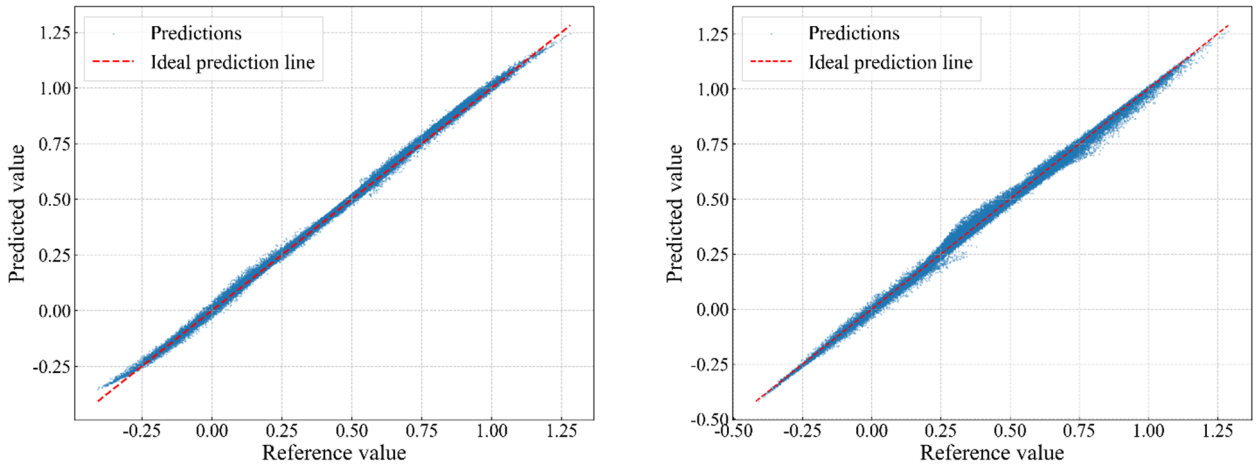
$$\begin{cases} y_H = \frac{1}{2}\left[0.1\exp(x_1 + x_2) - x_4 \sin(12\pi x_3) + x_3\right], & x_i \in (0,1], \quad i = 1,2,3,4 \\ y_L = 1.2y_H - 0.5 \end{cases} \tag{24}$$

To evaluate the uncertainty in the test cases, the Prediction Interval Coverage Probability (PICP) [28] is adopted as a metric:

$$\mathrm{PICP} = \frac{1}{\mathrm{N}} \sum_{\mathrm{n}=1}^{\mathrm{N}} \mathrm{c}_{\mathrm{n}} \tag{25}$$

Where N is the total number of predictions. If $y(x_n) \in [\tilde{y} - 2\sigma_n, \tilde{y} + 2\sigma_n]$, then $c_n = 1$; otherwise $c_n = 0$. Furthermore, $y(x_n)$ is the exact value of x_n and $\tilde{y}$ and σ_n represent the mean and standard deviation of the model's predicted output, respectively. Ideally, the closer the PICP is to 95%, the higher the accuracy of the prediction interval.

A total of 25,000 low-fidelity data points and 150 high-fidelity data points obtained by Latin Hypercube Sampling (LHS) are used for low-fidelity and high-fidelity training, respectively. The DNN used to approximate the low-fidelity data has two hidden layers with 50 neurons per layer; the BNN uses one hidden layer, also with 50 neurons. For validation, 100,000 random positions are selected to display the predictions of the multi-fidelity model and Co-Kriging. The prediction results are shown in Table 2 and Figure 4. Compared with Co-Kriging, MFBNN achieves higher prediction accuracy, and the PICP value is improved by approximately 10%, demonstrating the relative advantages of the multi-fidelity model in both prediction accuracy and uncertainty quantification.



(a) Comparison of MFBNN predicted values with true values

(b) Comparison of Co-Kriging predicted values with true values

Figure 4 – Regression with 4D test functions

Table 2 – Comparison of evaluation metrics for regression with 4D test function

Model	Correlation coefficient	PICP
MFBNN	0.9993	99.75%
Co-Kriging	0.9975	89.85%

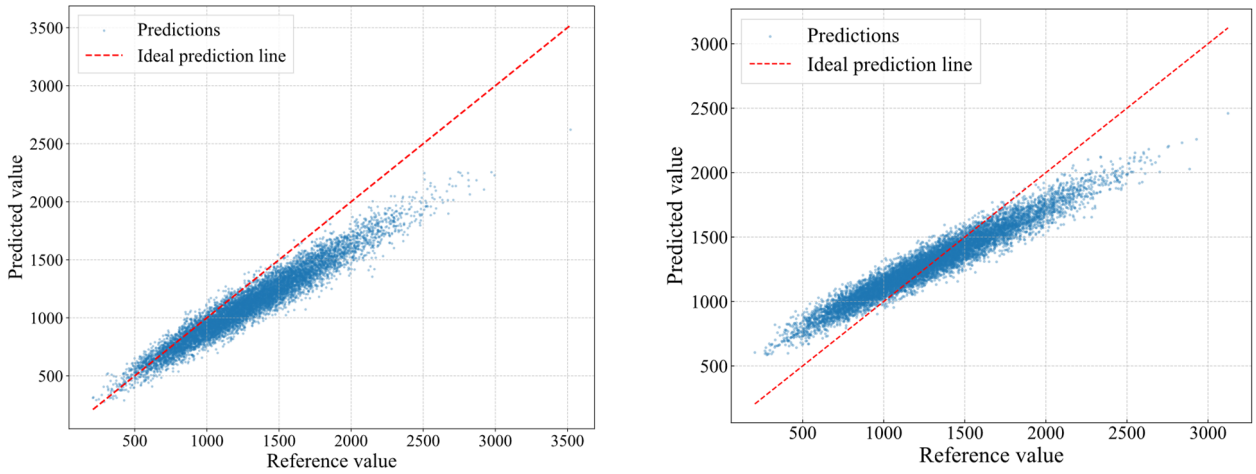
3.4 20D Test Function

Consider the following 20-dimensional function regression example:

$$\begin{cases} y_H = (x_1 - 1)^2 + \sum_{i=2}^{20} (2x_i^2 - x_{i-1})^2 \\ y_L = 0.8 y_H - \sum_{i=1}^{19} 0.4 x_i x_{i+1} - 50 \end{cases}, \quad x_i \in [-3, 3], i = 1, 2, \ldots, 20 \tag{26}$$

4,000 low-fidelity training data points and 500 high-fidelity training data points are randomly selected, along with 10,000 test data points.

The results in Table 3 and Figure 5 show that, at the 20-dimensional scale, the coefficient of determination of the MFBNN model is higher than that of Co-Kriging. The PICP values are 98.49% for MFBNN and 94.68% for Co-Kriging; therefore, Co-Kriging is slightly better calibrated by the PICP criterion alone because 94.68% is closer to the nominal 95% coverage. MFBNN nevertheless provides the higher R2 value, so interval calibration should be interpreted together with the point-prediction metrics rather than as a standalone claim of superiority. Moreover, the predicted points of MFBNN are closer to the ideal prediction line compared to Co-Kriging.



(a) Comparison of MFBNN predicted values with true values

(b) Comparison of Co-Kriging predicted values with true values

Figure 5 – Regression with 20D test functions

Table 3 – Comparison of evaluation metrics for regression with 20D test function

Model	Correlation coefficient	R^2	PICP
MFBNN	0.965448	0.932089	98.49%
Co-Kriging	0.9661	0.8226	94.68%

4. Stealth Characteristics Data Fusion

4.1 Numerical Analysis of Stealth Characteristics

In high-frequency and full-band electromagnetic calculations, PO and MoM serve as typical representatives of high-frequency approximation methods and rigorous numerical methods, respectively, exhibiting significant complementarity. PO achieves efficient computation through assumptions such as tangent plane approximation and shadow region neglect, making it suitable for electrically large targets. MoM, on the other hand, accurately solves for surface currents based on integral equations but suffers from high computational complexity for complex problems. To improve the scalability of the Method of Moments, the Multi-level Fast Multipole Method (MLFMM) has been developed by introducing the addition theorem, plane wave expansion theorem, and multilevel structures. It can fully capture the entire physical process of electromagnetic scattering and achieve accurate RCS calculation. However, this "high accuracy" comes with high computational cost. There exists a significant nonlinear relationship between PO and MLFMM data. The more complex the correlation between high- and low-fidelity data, the higher the requirement for model fitting accuracy and uncertainty quantification capability. The multi-layer neural network structure of MFBNN can autonomously learn these complex correlations, possessing the ability to learn such complex mappings, further demonstrating the advantages of the proposed model in highly nonlinear scenarios.

To validate the proposed method, the X47B-like low-observable aircraft configuration is adopted to verify the computational accuracy of the three-dimensional RCS evaluation method. The external dimensions of the X47B-like configuration are shown in Figure 6. The wingspan is 20.16 m, the half-model reference area (based on the single-wing planform) is 42.43 m², the reference center for aerodynamic evaluation is taken at $x = 6.17$ m, and the mean aerodynamic chord length is 3.32 m. The wing root section ($y = 0.0$ m) has a chord length of 11.6 m and a thickness ratio of 16%; the kink1 ($y = 4.5$ m) and kink2 ($y = 8.0$ m) sections have a chord length of 2.56 m and a thickness ratio of 11%; the wingtip section ($y = 10.08$ m) has a chord length of 0.2 m and a thickness ratio of 11%. Each section of the basic configuration is obtained by modifying the thickness of the symmetric airfoil NACA 65016[29].

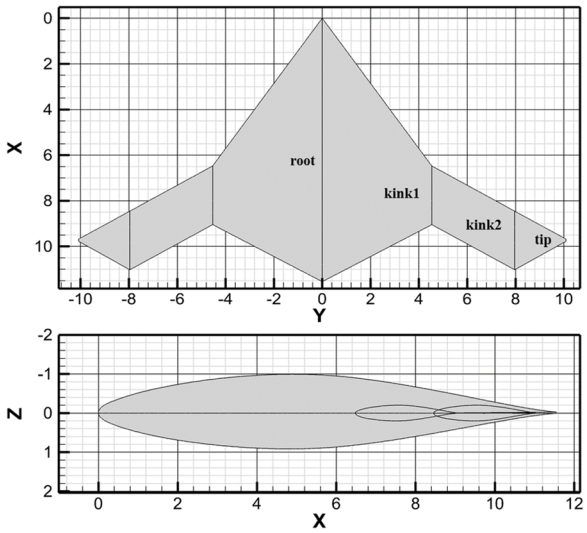
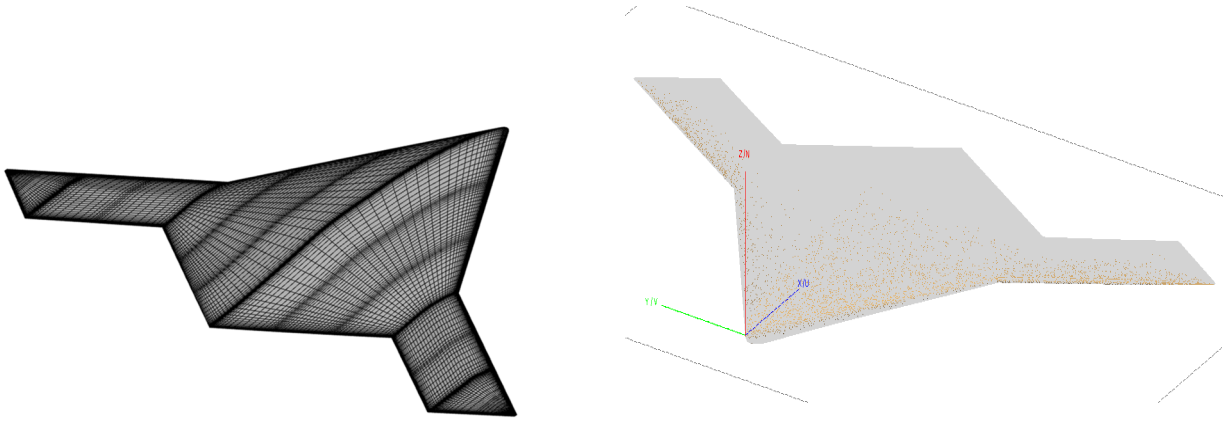


Figure 6 – Basic external geometry dimensions of X47B-like configuration

Different methods are used to solve for RCS in the computational electromagnetic simulation software FEKO. MLFMM, based on the Method of Moments, is a rigorous numerical method for solving Maxwell's integral equations, and its accuracy can be systematically controlled through mesh discretization. The MLFMM solver in FEKO has been extensively validated by the industry and is recognized as an authoritative tool for calculating RCS of complex targets. Therefore, the MLFMM results calculated in this paper can be approximated as true solutions. The radar wave incident frequency is set to $f = 1$ GHz, the far-field angle step is $1°$, and the average mesh size used is approximately $\lambda/8$. A schematic diagram of the mesh generation is shown in Figure 7.

The bistatic RCS under horizontal polarization is calculated in the x-y plane. The calculation results are shown in Figure 8. It can be observed that the X47B-like configuration exhibits RCS peaks at $\varphi = 30°$, $\varphi = 125°$, and $\varphi = 150°$. A comparison of computation time, mesh quantity, and the calculated mean RCS values for PO and MLFMM is shown in Table 4. The Physical Optics method takes only about 8.5 seconds, which is extremely fast, while the mesh quantity for the Multi-level Fast Multipole Method is 40 times larger than that for PO, directly demonstrating the difference in computational efficiency between the two methods. It is worth noting that the RCS values of PO are relatively small at most angles, with the mean RCS deviating by approximately -5.40 dBsm from the MLFMM result. This deviation is consistent with theoretical expectations, confirming that PO indeed ignores electromagnetic scattering characteristics such as edge diffraction and multiple scattering, thereby underestimating the contribution of local complex structures to the RCS of the target.



(a) PO mesh

(b) MLFMM mesh

Figure 7 – Schematic diagram of X47B-like configuration mesh generation

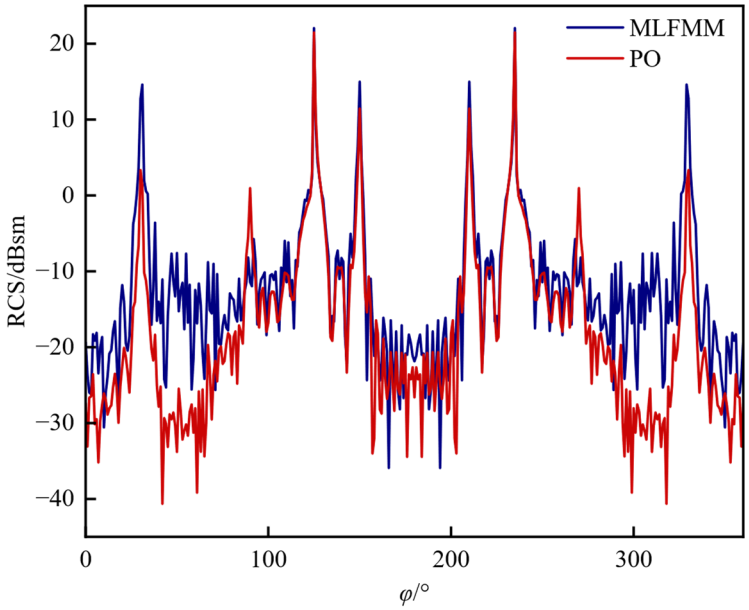


Figure 8 – RCS results of X47B-like configuration under horizontal polarization

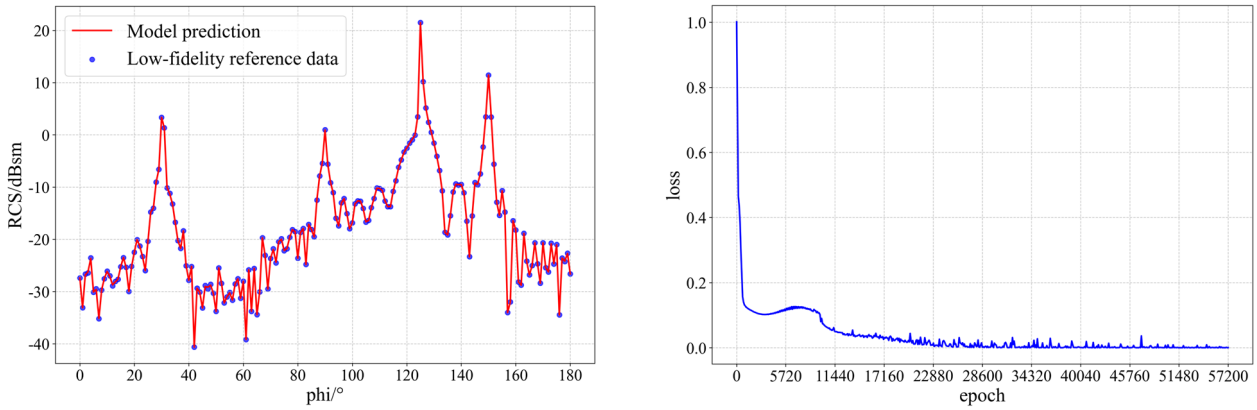
Table 4 – Calculation time and mesh quantity of X47B-like configuration

Method	Computation Time(s)	Mesh Quantity (10^4)	Mean RCS (dB)
PO	≈8.5	1.6	-18.21
MLFMM	≈2043	64	-12.81

4.2 Stealth Data Fusion Results

A case study is conducted based on the RCS results of the X47B-like configuration under horizontal polarization. Since the RCS is symmetric about the azimuth angle of 180°, data fusion is actually performed on the results within the range of 0-180°. From Table 4, the total sampling time for high-fidelity data within this range is approximately 1021.5 seconds. PO data are sampled at 1° azimuth intervals, yielding 180 low-fidelity samples. MLFMM data are sampled at 5° and 10° intervals, yielding 36 and 18 high-fidelity samples, respectively, with corresponding sampling times of 765.4 seconds and 440.5 seconds. Therefore, sampling 180 low-fidelity samples and 36 high-fidelity samples saves nearly 25% of the time compared to sampling 180 high-fidelity samples, while sampling 180 low-fidelity samples and 18 high-fidelity samples saves about 56.5% of the time, demonstrating the efficiency advantage of the multi-fidelity data fusion model.

The low-fidelity model requires modeling the 180 RCS results obtained by the PO method. The DNN hidden layer uses 5 layers with 512 neurons per layer. The final mean square error after model training is 0.000034. The prediction results and the loss curve during the training process are shown in Figure 9. After the low-fidelity model is trained, its predicted output, together with the MLFMM data input, is used as the input to the high-fidelity layer to train the high-fidelity model.

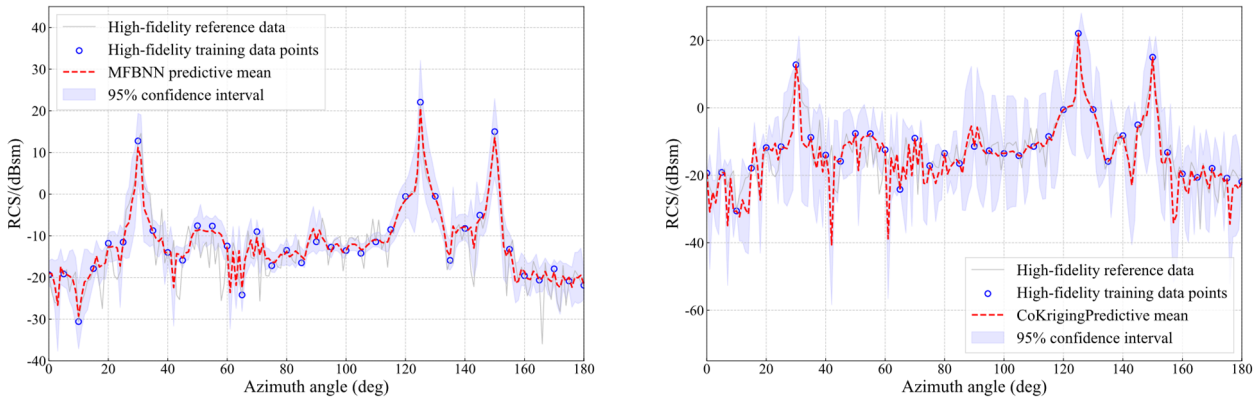


(a) Low-fidelity DNN prediction (b) Low-fidelity training loss curve

Figure 9 – Low-fidelity model prediction and loss curve diagram

In this section, 36 and 18 MLFMM calculation results are used as high-fidelity data, respectively, to investigate the performance of the models under different numbers of high-fidelity samples.

First, 36 high-fidelity data points (sampling interval of 5°) are used for modeling. The AdamW optimizer is employed, with the high-fidelity layer using 3 hidden layers containing 128 neurons each, the KL weight set to 0.0001, and the learning rate set to 0.001. Figure 10(a) shows the prediction results of the MFBNN model. It can be observed that the uncertainty is small near the high-fidelity training points and increases significantly in regions without high-fidelity data, which is consistent with physical intuition, indicating that the model can reasonably express the degree of uncertainty in its predictions when data are insufficient. Figure 10(b) shows the prediction results of the Co-Kriging model. This model fits the high-fidelity training data points extremely well but has poor predictive capability in regions outside the training points, exhibiting severe overfitting. From the core accuracy metrics in Table 5, the MSE of MFBNN is reduced by 47.71% compared to Co-Kriging, the RMSE is reduced by 27.70%, and the R^2 is improved by 32%. The error of the predicted mean RCS relative to the MLFMM benchmark (-12.81 dB) is about 6.79% for MFBNN, while the error for Co-Kriging is about 9.37%, indicating that MFBNN has significant advantages in prediction accuracy and generalization ability. Regarding interval calibration, Co-Kriging's PICP of 88.40% is closer to the nominal 95% coverage than MFBNN's 72.38%; it is therefore better calibrated by PICP in this case. The narrower MFBNN intervals should be interpreted together with coverage and point-prediction metrics, rather than described as superior on PICP alone.



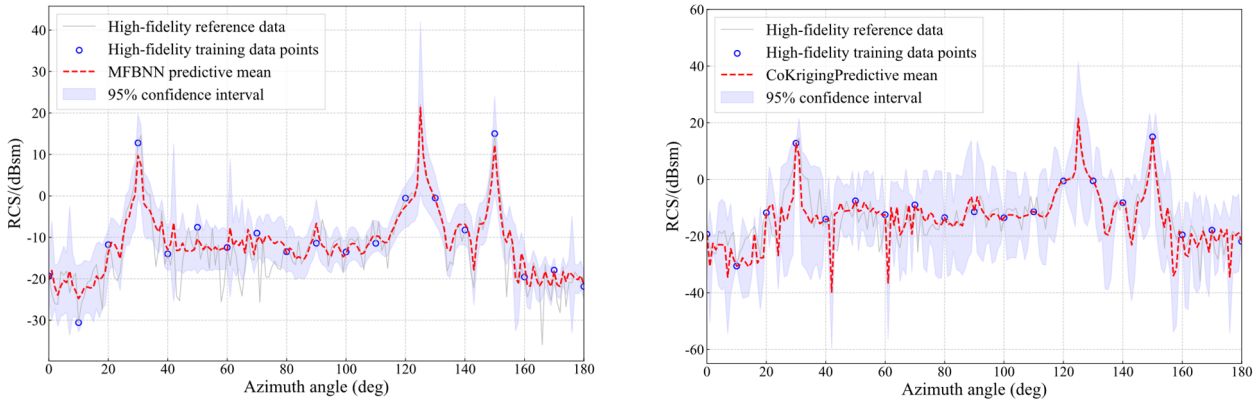
(a) MFBNN prediction results and uncertainty (b) Co-Kriging prediction results and uncertainty

Figure 10 – Prediction results for 36 high-fidelity data points

Table 5 – A comparison of evaluation metrics for 36 high-fidelity data points

Model	MSE	RMSE	R^2	Mean RCS (dB)	PICP (%)
MFBNN	0.1508	0.3883	0.7903	-11.94	72.38
Co-Kriging	0.2884	0.5371	0.5988	-14.01	88.40

When the high-fidelity data are reduced to 18 points (sampling interval of 10°), the number of neurons in the high-fidelity layer is adjusted to 32. The results are shown in Figure 11 and Table 6. Compared with the results from 36 data points, the mean square error of Co-Kriging increases from 0.2884 to 0.3111, an increase of about 7.87%, indicating that the covariance function fitting becomes unstable under sparse data, and the prediction results tend to deviate from the true values. In contrast, the prediction results of MFBNN remain almost unchanged from before, while the prediction intervals reasonably widen as the available data decrease, reflecting the stability of model predictions under small sample conditions and conservative estimation in data-deficient regions. In terms of mean RCS, both models show a slight increase in their predicted values due to the reduction in data volume.



(a) MFBNN prediction results and uncertainty

(b) Co-Kriging prediction results and uncertainty

Figure 11 – Prediction results for 18 high-fidelity data points

Table 6 – A comparison of evaluation metrics for 18 high-fidelity data points

Model	MSE	RMSE	R^2	Mean RCS (dB)	PICP (%)
MFBNN	0.1680	0.4098	0.7664	-11.51	84.53
Co-Kriging	0.3111	0.5577	0.5673	-13.82	90.61

In summary, in terms of prediction accuracy, MFBNN implicitly learns the complex nonlinear relationships between high- and low-fidelity data through neural networks, while Co-Kriging relies on explicit covariance assumptions and lacks flexibility in nonlinear scenarios. Under small dataset conditions, MFBNN provides risk-controllable predictions through uncertainty quantification while maintaining prediction accuracy, whereas Co-Kriging has potential biases. Therefore, in multi-fidelity modeling, MFBNN performs better than the traditional Co-Kriging method, especially in scenarios with sparse data and strong nonlinearity, where its accuracy, robustness, and uncertainty quantification capability have greater engineering practical value.

5. Aerodynamic Characteristics Data Fusion

5.1 Multi-fidelity Data Sources

In data fusion learning and modeling, numerical calculation results are used as low-fidelity data, while wind tunnel test results are used as high-fidelity data. High-precision experimental measurements often cannot capture all flow field details, and obtaining such data is difficult, expensive, and very limited. In contrast, although numerical calculation methods cannot achieve the accuracy of experiments, they can easily obtain global flow field information.

The wind tunnel test data provided by the NACA0012 airfoil 9218 case in the NASA report[30, 31] are selected for validation, and the aerodynamic response of the airfoil under unsteady pitching motion is simulated. This case is a classic dynamic stall case with high-dimensional nonlinear response characteristics, making it suitable as a benchmark for validating multi-fidelity modeling. The motion parameters and freestream velocity are set as follows:

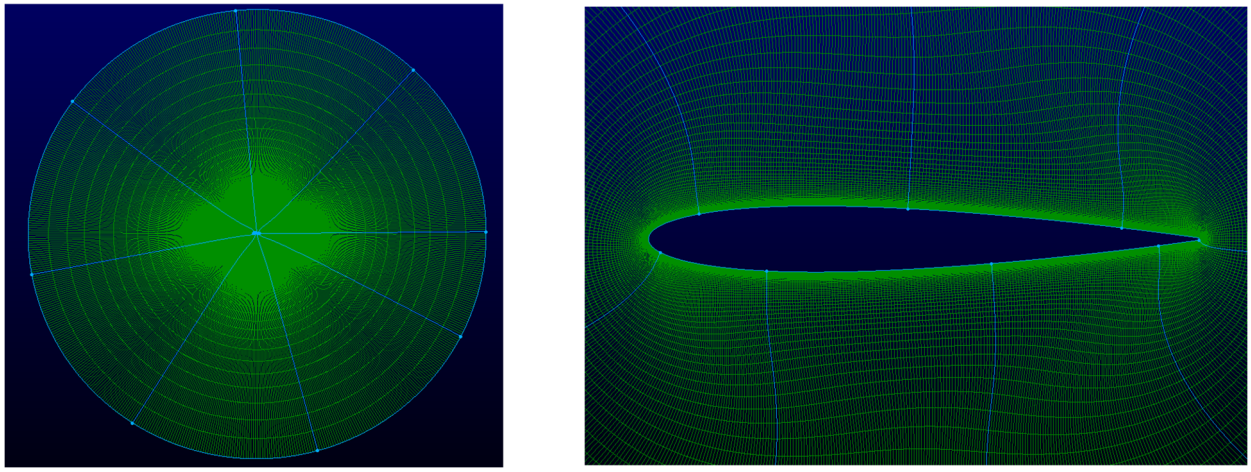
$$\alpha = \alpha_0 + \alpha_m \sin(\omega t) \tag{27}$$

Where $Ma = 0.283$, $Re = 3.45 \times 10^6$, $\alpha_0 = 14.91$, $\alpha_m = 9.88$, $kr = 0.151$. The angular frequency ω can be derived from the relationship of kr:

$$\omega = 2 \cdot \mathrm{kr} \cdot U_\infty / c \tag{28}$$

Where U_∞ is the freestream velocity and c is the airfoil chord length. This setup simulates the periodic pitching motion of the airfoil about its quarter-chord, representing a typical unsteady flow condition that induces dynamic lift variations.

Validated coupled Delayed Detached Eddy Simulation and Transitional Delayed Detached Eddy Simulation (TDDES) models with transition prediction are used for unsteady numerical simulations. The calculation results are used as low-fidelity data. A schematic diagram of the NACA0012 mesh is shown in Figure 12, with a mesh size of 197,056. The experimental data are used as high-fidelity data.

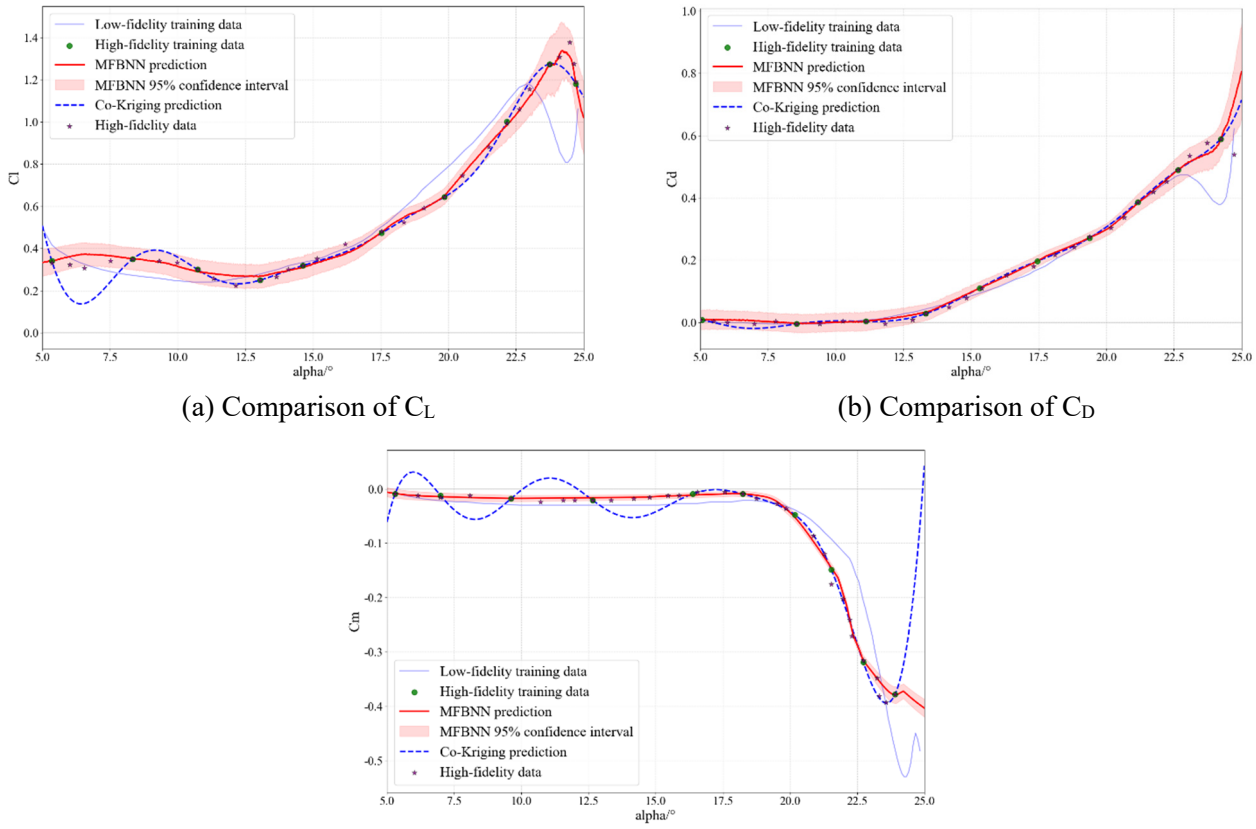


(a) Overview (b) Close-up view

Figure 12 – Schematic diagram of NACA0012 airfoil mesh generation

5.2 Aerodynamic Data Fusion Results

A total of 612 low-fidelity samples and 10 high-fidelity samples are uniformly selected to train the MFBNN model. After the model training is completed, the MFBNN model is used to predict each input point. Multiple output instances are obtained through Monte Carlo sampling, and their mean and standard deviation are calculated as the prediction value and confidence estimate, respectively. The differences in the three curves of lift coefficient, drag coefficient, and moment coefficient with respect to angle of attack among the numerical calculation results, experimental data, and model prediction results are compared (Figure 13).



(a) Comparison of C_L

(b) Comparison of C_D

(c) Comparison of C_M

Figure 13 – Comparison diagram of NACA0012 airfoil aerodynamic coefficient predictions

The comparison results show that the predicted mean of the MFBNN model is closer to the experimental results, and the error is significantly reduced compared to the calculation error of the TDDES model. The prediction results of lift coefficient and moment coefficient are significantly better than those of the traditional Co-Kriging model. Moreover, the confidence interval of MFBNN basically covers all high-fidelity validation data, keeping the error within two standard deviations, demonstrating the rationality of the model in uncertainty quantification. Compared with the single-value prediction of TDDES, the MFBNN model provides better uncertainty estimation capability.

6. Conclusions

This work makes following main contributions:

- The multi-fidelity Bayesian neural network proposed in this paper adopts a hierarchical architecture consisting of a low-fidelity deep neural network and a high-fidelity Bayesian neural network, which can learn highly nonlinear cross-fidelity correlations without requiring preset correlation assumptions, unlike Co-Kriging. Considering the limitations of high-precision MCMC posterior inference methods in terms of efficiency and scalability, this paper employs VI to approximate the complex true posterior in Bayesian inference, greatly improving feasibility for large-scale problems. However, the current VI method is inherently an approximation process. Even when made as close as possible to the true posterior distribution, it still falls short of capturing complex characteristics such as multimodality. Future work should explore more flexible posterior approximation methods based on the current research to better capture the complex structure of the true posterior while maintaining computational efficiency;

- In the multi-source stealth electromagnetic characteristic scenario, taking the three-dimensional X47B flying-wing configuration as an example, MFBNN fuses high-precision MoM data with low-precision PO data. Under different high-fidelity sample sizes, MFBNN exhibits lower prediction

error and higher goodness of fit compared to the Co-Kriging model, significantly reducing the dependence on high-fidelity samples and effectively resolving the inherent trade-off between accuracy and efficiency in traditional electromagnetic numerical computations. Meanwhile, the Co-Kriging model exhibits severe overfitting under small sample conditions, failing to capture the true trend of the data at points far from the training points. In contrast, the uncertainty provided by MFBNN converges near the training points and reasonably expands in extrapolation regions, which is more reasonable than the redundant predictions of Co-Kriging, highlighting the advantages of MFBNN in prediction accuracy and uncertainty estimation;

- In the aerodynamic characteristic data fusion scenario, taking the unsteady aerodynamic force prediction of the NACA0012 airfoil as an example, MFBNN fuses aerodynamic numerical calculation results with wind tunnel test data, using lift coefficient, drag coefficient, and moment coefficient as core evaluation metrics. The predicted mean of MFBNN is closer to the experimental observations than the prediction results of the TDDES model and Co-Kriging, and the confidence intervals can reasonably reflect the uncertainty of the predictions, covering most of the actual observations. The results demonstrate the cross-disciplinary generalization capability of the proposed model from electromagnetics to aerodynamics. Future work can provide quantitative basis for robust decision-making in aerodynamic-stealth integrated design and multidisciplinary optimization.

7. Contact Author Email Address

Corresponding author email: jiayihe@mail.nwpu.edu.cn

8. Copyright Statement

The authors confirm that they, and/or their company or organization, hold copyright on all of the original material included in this paper. The authors also confirm that they have obtained permission, from the copyright holder of any third party material included in this paper, to publish it as part of their paper. The authors confirm that they give permission, or have obtained permission from the copyright holder of this paper, for the publication and distribution of this paper as part of the ICAS proceedings or as individual off-prints from the proceedings.

References

[1] Myers R H, Montgomery D C, Anderson-Cook C M. Response surface methodology: process and product optimization using designed experiments[M]. John Wiley & Sons, 2016.

[2] Brereton R G, Lloyd G R. Support vector machines for classification and regression[J]. Analyst, 2010,135(2):230-267.

[3] Cressie N. Statistics for spatial data[M]. John Wiley & Sons, 2015.

[4] Espoeys R, Brevault L, Balesdent M, Ricci S, Mycek P. Multi-fidelity sequential Bayesian optimization and reliability assessment method for the design of complex systems[C]. 5th ECCOMAS Thematic Conference on Uncertainty Quantification in Computational Science and Engineering (UNCECOMP 2023), Athens, Greece, 12-14 June 2023. ECCOMAS Proceedia, 2023:125-150.

[5] Zhang Y, Gong Z, Zhou W, et al. Multi-fidelity surrogate modeling for temperature field prediction using deep convolution neural network[J]. Engineering Applications of Artificial Intelligence, 2023,123:106354.

[6] Jofre L, Papadakis M, Roy P T, Aiken A, Iaccarino G. Multifidelity modeling of irradiated particle-laden turbulence subject to uncertainty[J]. International Journal for Uncertainty Quantification, 2020,10(6):499-514. doi:10.1615/Int.J.UncertaintyQuantification.2020032236.

[7] Wang X, Ning C, Wang W, et al. An intelligent fusion method for multi-source aerodynamic data in flight tests[J]. Acta Aerodynamica Sinica, 2023,41(2):12-20.

[8] Zhao X, Zhang W, Deng Z. Aerodynamic modeling method incorporating pressure distribution information[J]. Chinese Journal of Theoretical and Applied Mechanics, 2022,54(9):2616-2626.

[9] Peng X, Kou J, Zhang W. Multi-fidelity nonlinear unsteady aerodynamic modeling and uncertainty estimation based on Hierarchical Kriging[J]. Applied Mathematical Modelling, 2023,122:1-21.

[10] Li K, Kou J, Zhang W. Deep learning for multifidelity aerodynamic distribution modeling from experimental and simulation data[J]. AIAA Journal, 2022,60(7):4413-4427.

[11] Park C, Haftka R T, Kim N H. Remarks on multi-fidelity surrogates[J]. Structural and Multidisciplinary Optimization, 2017,55(3):1029-1050.

[12] Zhou Q, Wu J, Xue T, et al. A two-stage adaptive multi-fidelity surrogate model-assisted multi-objective genetic algorithm for computationally expensive problems[J]. Engineering with computers, 2021,37(1):623-639.

[13] Liu J, Yang K, Jiang J, Xia B. Parameter estimation method of equipment system based on multi-fidelity surrogate model[J]. Systems Engineering and Electronics, 2021,43(1):130-137.

[14] Zhu J, Wang Y J, Collette M. A multi-objective variable-fidelity optimization method for genetic algorithms[J]. Engineering Optimization, 2014,46(4):521-542.

[15] Liu Y, Collette M. Improving surrogate-assisted variable fidelity multi-objective optimization using a clustering algorithm[J]. Applied Soft Computing, 2014,24:482-493.

[16] Zhang H, Chen Z, Li Y. Efficient design optimization and experimental verification of shaped film cooling holes based on multi-fidelity surrogate models[J]. Journal of Engineering Thermophysics, 2020,41(1):128-134.

[17] Zhang W, Feng F, Liu W, et al. Advanced parallel space-mapping-based multiphysics optimization for high-power microwave filters[J]. IEEE transactions on microwave theory and techniques, 2021,69(5):2470-2484.

[18] Kennedy M C, O'Hagan A. Predicting the output from a complex computer code when fast approximations are available[J]. Biometrika, 2000,87(1):1-13.

[19] Chung H S, Choi S, Alonso J J. Design of a low-boom supersonic business jet using evolutionary algorithms and an adaptive unstructured mesh method[C]. 22nd Applied Aerodynamics Conference, Providence, RI, USA, 16-19 August 2004. AIAA Paper 2004-1758.

[20] Zhang M, Jiao J, Zhang J, et al. High-Efficiency Data Fusion Aerodynamic Performance Modeling Method for High-Altitude Propellers[J]. Drones, 2024,8(6):229.

[21] Huang L, Gao Z, Zhang D. Research on multi-fidelity aerodynamic optimization methods[J]. Chinese Journal of Aeronautics, 2013,26(2):279-286.

[22] Meng X, Karniadakis G E. A composite neural network that learns from multi-fidelity data: Application to function approximation and inverse PDE problems[J]. Journal of Computational Physics, 2020,401:109020.

[23] Li S, Xing W, Kirby R, et al. Multi-fidelity Bayesian optimization via deep neural networks[J]. Advances in Neural Information Processing Systems, 2020,33:8521-8531.

[24] Lee E S, Zhou L, Ribeiro A, et al. Graph neural networks for decentralized multi-agent perimeter defense[J]. Frontiers in Control Engineering, 2023,4:1104745.

[25] Xie F, Zhang X, Wu S, et al. Multi-fidelity Bayesian neural networks for aerodynamic data fusion with heterogeneous uncertainties[J]. Computer Methods in Applied Mechanics and Engineering, 2025,435:117666.

[26] Vaiuso A, Immordino G, Righi M, et al. Multi-Fidelity Bayesian Neural Network for Uncertainty Quantification in Transonic Aerodynamic Loads[J]. arXiv preprint arXiv:2407.05684, 2024.

[27] Yang L, Meng X, Karniadakis G E. B-PINNs: Bayesian physics-informed neural networks for forward and inverse PDE problems with noisy data[J]. Journal of Computational Physics, 2021,425:109913.

[28] Yao J, Pan W, Ghosh S, et al. Quality of uncertainty quantification for Bayesian neural network inference[J]. arXiv preprint arXiv:1906.09686, 2019.

[29] Zhou L. Research on aerodynamic-stealth integrated design of low observable configurations based on global/gradient coupling methodology[D]. Northwestern Polytechnical University, 2022.

[30] Landon R H. NACA 0012 oscillatory and transient pitching[R]. Data Set 3 in Compendium of Unsteady Aerodynamic Measurements, AGARD-R-702. Advisory Group for Aerospace Research and Development (AGARD), North Atlantic Treaty Organization, 1982:68-92.

[31] Wood M E. Results of oscillatory pitch and ramp tests on the NACA 0012 blade section[R]. ARA Memo No. 220. Aircraft Research Association Ltd., Bedford, UK, December 1979.